BEILSTEIN JOURNAL OF NANOTECHNOLOGY

Polymer-mediated surface engineering enables directional growth of RuO_2 nanorods on electrospun V_2O_5 nanofibers

Jiwoo Song[‡1], Namhee Kim[‡1,2], Minjae Kim[3], Myung Hwa Kim[*1,2] and Dasol Jin[*3]

Full Research Paper

Open Access

Address:
[1]Department of Chemistry & Nanoscience, Ewha Womans University, Seoul 03760, Republic of Korea, [2]Institute of Multiscale Matter and System (IMMS), Ewha Womans University, Seoul 03760, Republic of Korea and [3]Department of Chemistry, Jeonbuk National University, Jeonju 54896, Republic of Korea

Email:
Myung Hwa Kim[*] - myungkim@ewha.ac.kr;
Dasol Jin[*] - dasoljin@jbnu.ac.kr

* Corresponding author ‡ Equal contributors

Keywords:
anisotropic crystal growth; electrospinning; polymer engineering; RuO_2 nanorods; V_2O_5 nanofibers

Beilstein J. Nanotechnol. **2026,** *17,* 1566–1573.
https://doi.org/10.3762/bjnano.17.106

Received: 23 July 2026
Accepted: 27 October 2026
Published: 04 November 2026

Associate Editor: A. Gölzhäuser

© 2026 Song et al.; licensee Beilstein-Institut.
License and terms: see end of document.

Abstract

Controlling the morphology of metal oxide nanostructures through simple and scalable synthetic strategies remains challenging because crystal growth is strongly governed by interfacial surface chemistry. Herein, we present a polymer-mediated strategy for directing the growth of RuO_2 nanorods on electrospun V_2O_5 nanofibers by tuning the polyvinylpyrrolidone (PVP)/polyacrylonitrile (PAN) ratio in the precursor solution. PAN incorporation preserves the one-dimensional V_2O_5 framework while progressively promoting the formation of vertically aligned RuO_2 nanorods. Structural and spectroscopic analyses reveal that PAN-induced thermal evolution modifies the surface chemistry of V_2O_5 by increasing pyridinic nitrogen functionalities and oxygen-deficient surface sites. These surface characteristics are proposed to facilitate preferential Ru precursor nucleation, leading to anisotropic crystal growth without altering the crystal structures of either V_2O_5 or RuO_2. The optimized composition containing 50 wt % PAN exhibits the most homogeneous and vertically aligned RuO_2 nanorod arrays.

Introduction

Controlling crystal growth at heterogeneous oxide interfaces remains a fundamental challenge because nucleation and morphological evolution are highly sensitive to the local chemical environment during thermal processing [1]. Although numerous synthetic approaches have been developed to regulate metal oxide nanostructures, precise control over anisotropic crystal growth generally relies on surfactants, templates, or complex solution chemistries that limit scalability and synthetic simplicity [2]. Vanadium oxides (VO_x, x = 1.0–2.5) exhibit multiple accessible oxidation states (V^{3+}, V^{4+}, and V^{5+}), enabling reversible redox reactions for a wide range of electrochemical energy-storage and conversion applications [3-7]. Despite these advantages, their relatively poor electrical conductivity often limits reaction kinetics and overall electro-

chemical performance. Hybridization with highly conductive noble metal oxides provides an attractive strategy to overcome these limitations by simultaneously improving charge transport and interfacial electron transfer. Among various candidates, RuO_2 is particularly attractive owing to its metallic conductivity, excellent chemical stability and fast surface redox kinetics, making it one of the most efficient oxide materials for electrocatalysis [8,9], electrochemical sensing [10-12], and heterogeneous catalytic processes [13,14].

Existing synthetic approaches predominantly rely on surfactants, templates, or ligands to manipulate crystal growth [15,16]. While these methods effectively control morphology, they often increase synthetic complexity and provide limited control over the coupled evolution of oxide supports and secondary crystal nucleation during thermal processing. Consequently, developing a simple and scalable strategy that regulates crystal growth through intrinsic interfacial chemistry, rather than external structure-directing agents, remains highly desirable. In this regard, polymer-assisted electrospinning provides a unique opportunity to regulate interfacial chemistry during oxide formation [17,18]. Beyond controlling the morphology of precursor fibers, polymer composition governs the thermal evolution of the precursor matrix, thereby determining the formation of residual surface functionalities and defect structures after calcination. These polymer-derived surface characteristics can significantly influence heterogeneous nucleation and subsequent crystal growth; however, their role in directing the morphology of secondary metal oxides remains largely unexplored [19].

Herein, we demonstrate that polymer composition can be exploited to direct the anisotropic growth of RuO_2 nanorods on electrospun V_2O_5 nanofibers. By systematically tuning the polyvinylpyrrolidone (PVP)/polyacrylonitrile (PAN) ratio, the thermal evolution of the precursor fibers is regulated while preserving the one-dimensional V_2O_5 framework after calcination. The resulting polymer-derived surface chemistry, characterized by increased pyridinic nitrogen functionalities and oxygen-deficient surface sites, is proposed to facilitate preferential Ru precursor nucleation and anisotropic crystal growth, leading to uniformly aligned nanorods without altering the crystal structures of either V_2O_5 or RuO_2.

Experimental

Materials

Vanadium(III) chloride (VCl_3, 97%), ruthenium(III) chloride hydrate ($RuCl_3{\cdot}xH_2O$), polyvinylpyrrolidone (PVP, $M_W \approx 1\,300\,000$) and polyacrylonitrile (PAN, $M_W \approx 150\,000$) were purchased from Sigma-Aldrich (St. Louis, MO, USA). *N*,*N*-dimethylformamide (DMF, extra pure grade), ethanol (94.5%, extra pure grade), and sodium hydroxide (NaOH) beads were purchased from Ducksan (Korea). All other chemicals used were of analytical grade without further purification, and all solutions used for experiments were prepared with deionized water (resistivity ≥ 18 MΩ·cm).

Synthesis

Vanadium oxide nanofibers were synthesized via electrospinning followed by post-annealing, and the resulting samples were denoted as VF(x), where x represents the PAN weight percentage (wt %) in the precursor polymer composition. For VF(0), total of 50 mg of metal precursors were dissolved in a 1:1 (v/v) mixture of ethanol and deionized water. The resulting solution was ultrasonicated for 10 min, and then 300 mg of PVP was added. The mixture was stirred at 25 °C for 24 h to ensure complete homogenization and viscosity optimization for electrospinning. The as-prepared solution was then loaded into 12 mL plastic syringe fitted with a 25-gauge needle. Electrospinning (NanoNC ESR200R2) was performed under the following conditions: flow rate of 5 μL·min^{-1}, applied voltage of 15.0 kV, and needle-to-collector distance of 11 cm. VF(30), VF(50), VF(70), and VF(100) were prepared by incorporating PAN at 30, 50, 70, and 100 wt %, respectively. All the resulting as-spun nanofibers were calcined at 350 °C under a gas flow of 20 sccm O_2 and 80 sccm He, with ramping rate of 0.5 °C·min^{-1}. After synthesizing the VF(x) samples, amorphous ruthenium hydroxide (i.e., $Ru(OH)_y$) was prepared by the dropwise addition of 0.1 M NaOH to an aqueous $RuCl_3{\cdot}xH_2O$ solution until the pH reached 10 at 25 °C. The resulting precipitate was thoroughly washed with deionized water and redispersed in ethanol to form a homogeneous suspension. The $Ru(OH)_y$ suspension was then drop-cast onto the VF(x) substrates, followed by drying for 30 min. Subsequently, the samples were annealed in air at 200 °C for 3 h to obtain RuO_2. The resulting composites were denoted as RuO_2–VF(x).

Physical characterization

Morphological and elemental analyses were conducted via field-emission scanning electron microscopy (FESEM, JEOL JSM-7610F). High-resolution structural features were examined using high-resolution transmission electron microscopy (HRTEM, FEI Tecnai F20) and transmission electron microscopy (TEM, JEOL JEM-ARM200F NEOARM). Surface chemical states were investigated by angle-resolved X-ray photoelectron spectroscopy (ARXPS, Thermo Fisher Scientific K-ALPHA XPS, Al Kα radiation at 12 kV) and vibrational properties were probed using Raman microscope (HORIBA LabRAM HR Evolution 800). Thermal analysis was conducted with simultaneous thermogravimetric and differential thermal analysis (TGA-DSC, TA instruments STD 650) with a heating rate of 10 °C·min^{-1} up to 800 °C in air. Crystal structures were

analyzed by X-ray diffraction (XRD; Malvern Panalytical) using Cu Kα radiation (λ = 1.5406 Å).

Results and Discussion

To elucidate the influence of polymer composition on the growth behavior of RuO_2, the morphology and microstructure of the RuO_2–VF(x) composites were systematically characterized. The corresponding fabrication scheme is shown in Figure 1. SEM images (Figure 2a–e) reveal that the electrospun V_2O_5 nanofiber framework is well preserved over the entire PAN composition range, indicating that the incorporation of PAN effectively suppresses structural collapse during thermal processing. In the absence of PAN (RuO_2–VF(0), Figure 2a), RuO_2 is randomly deposited as discontinuous particulate aggre-

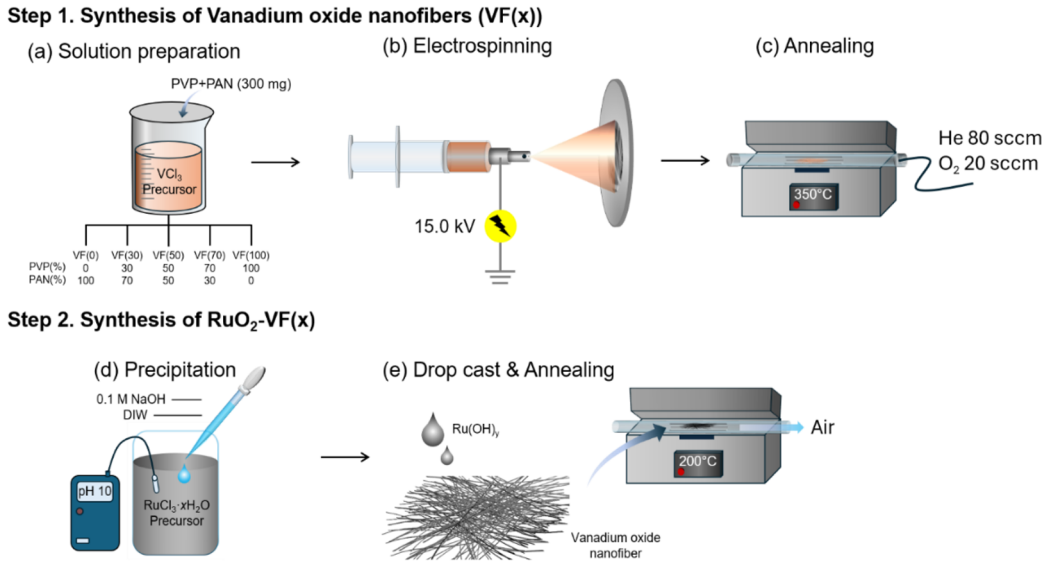


Figure 1: Schematic illustration of the synthetic methodology for RuO_2–VF(x) nanostructures.

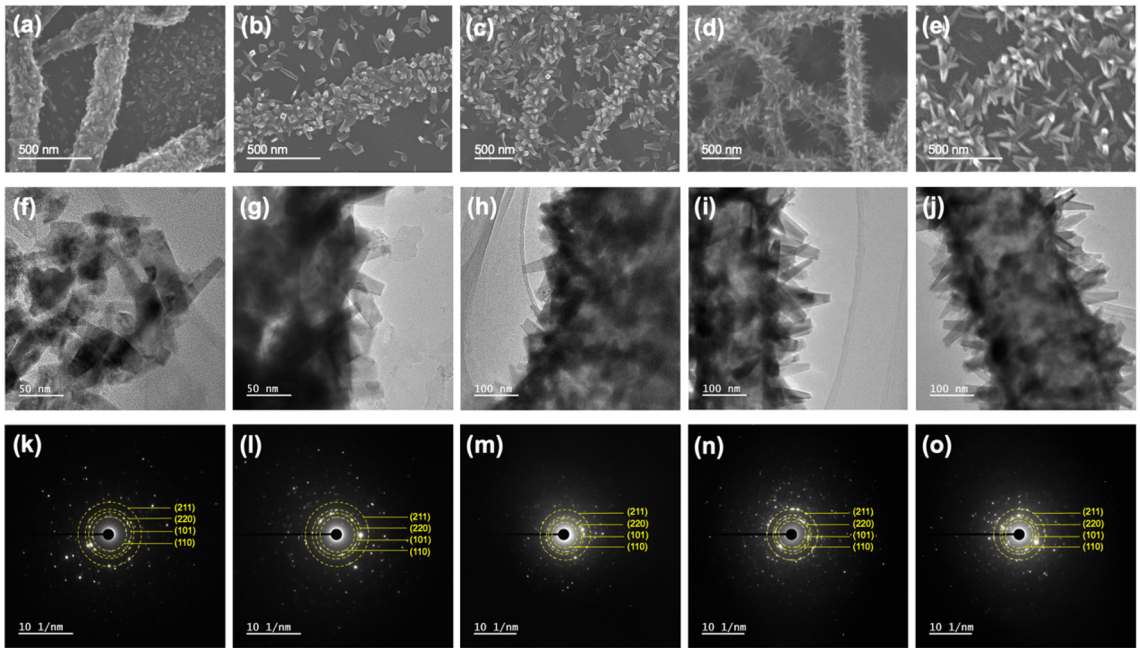


Figure 2: Morphological evolution of RuO_2 nanorods on electrospun V_2O_5 nanofibers with increasing PAN content (from left to right: x = 0, 30, 50, 70, and 100 wt %): (a–e) SEM images, (f–j) corresponding TEM images, and (k–o) SAED patterns of RuO_2–VF(x). The diffraction rings are indexed to the (110), (101), (220), and (211) planes of rutile RuO_2 (JCPDS No. 65-2824).

gates on the nanofiber surface, suggesting that crystal nucleation occurs isotropically without a preferred growth direction [20,21]. Upon increasing the PAN content, however, the RuO_2 growth mode gradually transitions from randomly distributed nanoparticles to vertically aligned nanorods: At 30 wt % PAN, elongated RuO_2 nanorods become discernible, while increasing the PAN content to 50 wt % results in densely packed and uniformly aligned nanorod arrays covering the V_2O_5 nanofiber surface. Further increasing the PAN content to 70 and 100 wt % produces no significant changes in nanorod morphology, indicating that the conditions favoring anisotropic RuO_2 growth are achieved at approximately 50 wt % PAN.

TEM observations (Figure 2f–j) further corroborate the SEM results by revealing the microstructural evolution of the RuO_2 coating. While RuO_2–VF(0) exhibits a discontinuous layer of randomly distributed nanoparticles, PAN incorporation promotes the formation of radially oriented RuO_2 nanorods with progressively improved uniformity and alignment. The RuO_2–VF(50) sample displays the most homogeneous nanorod architecture, supporting the conclusion that polymer composition governs the transition from isotropic particle deposition to anisotropic crystal growth. The crystal structure of the deposited RuO_2 was further examined by selected-area electron diffraction (SAED) (Figure 2k–o). All samples exhibit well-defined diffraction rings indexed to the (110), (101), (220), and (211) planes of rutile RuO_2 (JCPDS No. 65-2824), confirming the formation of crystalline RuO_2 regardless of PAN content. Despite the significant morphological evolution observed by SEM and TEM, the diffraction patterns remain essentially unchanged, indicating that polymer modulation regulates the nucleation and growth behavior of RuO_2 without altering its intrinsic crystal structure. To further investigate the elemental distribution within the RuO_2–V_2O_5 nanostructures, TEM-EDS elemental mapping was performed on RuO_2–VF(0) and RuO_2–VF(50) as representative samples (Supporting Information File 1, Figure S1 and Figure S2). Consistent with the SEM observations, RuO_2–VF(0) exhibits a rough surface, whereas RuO_2–VF(50) features distinct RuO_2 nanorods grown on V_2O_5 nanofibers. The detection of C, Ru, N, and V in both samples further supports the formation of RuO_2/V_2O_5 heterostructures. The XRD patterns in Figure S3 (Supporting Information File 1) show characteristic reflections of rutile RuO_2, indexed to the (110), (101), (220), and (211) planes (JCPDS No. 65-2824), consistent with the TEM-SAED results. The VF(100) PVP-100 sample exhibits relatively lower peak intensity than the PAN/PVP mixed and PAN-only samples.

To elucidate the structural characteristics of the V_2O_5 substrate governing the subsequent growth of RuO_2 nanorods, Raman spectroscopy was performed on the synthesized VF(x) nanofibers (Figure 3). All samples exhibit the characteristic Raman modes of orthorhombic α-V_2O_5, confirming the successful formation of the crystalline V_2O_5 framework regardless of polymer composition. The characteristic bands at approximately 142, 192, 284, 405, 698, and 994 cm^{-1} are assigned to the B_1g/B_3g lattice vibration, Ag/B_2g vanadium vibration, V–O bending, Ag V–O rocking, B_2g V–O stretching, and terminal V=O stretching modes, respectively, in good agreement with previous reports [22-25]. Notably, the positions of these characteristic Raman bands remain essentially unchanged from VF(0) to VF(70), indicating that increasing the PAN content does not alter the crystal structure of the electrospun V_2O_5 nanofibers. Although VF(100) exhibits reduced peak intensity accompanied by an increased spectral background, the characteristic α-V_2O_5 Raman modes remain clearly identifiable, suggesting that the crystalline framework is largely preserved even at the highest PAN content. These results demonstrate that modulation of the PVP/PAN ratio primarily influences the surface characteristics of the nanofibers without inducing phase transformation of the V_2O_5 substrate.

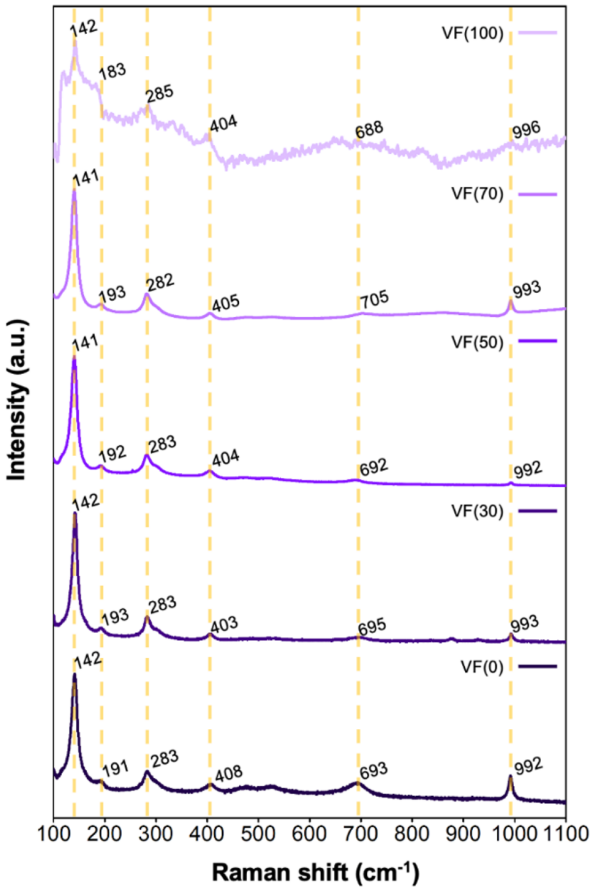


Figure 3: Raman spectra of electrospun V_2O_5 nanofibers (VF(x)) with increasing PAN content (x = 0, 30, 50, 70 and 100 wt %), demonstrating the preservation of the orthorhombic α-V_2O_5 structure.

To understand how polymer composition influences the growth behavior of RuO_2 nanorods, the thermal evolution of the as-spun VF(x) nanofibers was investigated by thermogravimetric analysis (TGA) and differential scanning calorimetry (DSC) in air (Figure 4). A notable feature observed in both TGA and DSC is the nearly identical thermal profiles of VF(x) with PAN contents of 50–100 wt %, which coincide with the saturation of the RuO_2 morphology observed by SEM and TEM (vide supra). This correlation suggests that the thermal evolution of the polymer matrix plays a critical role in establishing the interfacial chemical environment that governs the nucleation and anisotropic growth of RuO_2. As shown in Figure 4a, all samples exhibit an initial weight loss below 100 °C, which is attributed to the evaporation of residual solvent and physically adsorbed moisture. The thermal decomposition behavior thereafter strongly depends on polymer composition. VF(0), consisting solely of PVP, exhibits two major weight-loss events at approximately 330 and 445 °C, accompanied by corresponding exothermic peaks in the DSC profile (Figure 4b), which are associated with PVP side-chain decomposition and backbone combustion [26]. In contrast, PAN-containing samples exhibit distinctly different thermal characteristics. For VF(30), new exothermic events emerge at approximately 300 and 370 °C, corresponding to oxidative cyclization of nitrile groups and subsequent aromatization of the polymer backbone, respectively [27,28]. These reactions progressively dominate the thermal behavior as the PAN content increases, leading to nearly identical thermal profiles for VF(50–100). Importantly, the oxidative stabilization occurring near 300 °C takes place within the calcination temperature range employed for V_2O_5 nanofiber synthesis. The formation of a thermally stable ladder-like structure during this process is expected to suppress structural relaxation of the precursor fibers while simultaneously modifying the chemical environment of the oxide surface. The close agreement between the thermal evolution and the morphology of the resulting RuO_2 suggests that PAN-derived thermal stabilization contributes to the formation of surface conditions favorable for anisotropic RuO_2 growth.

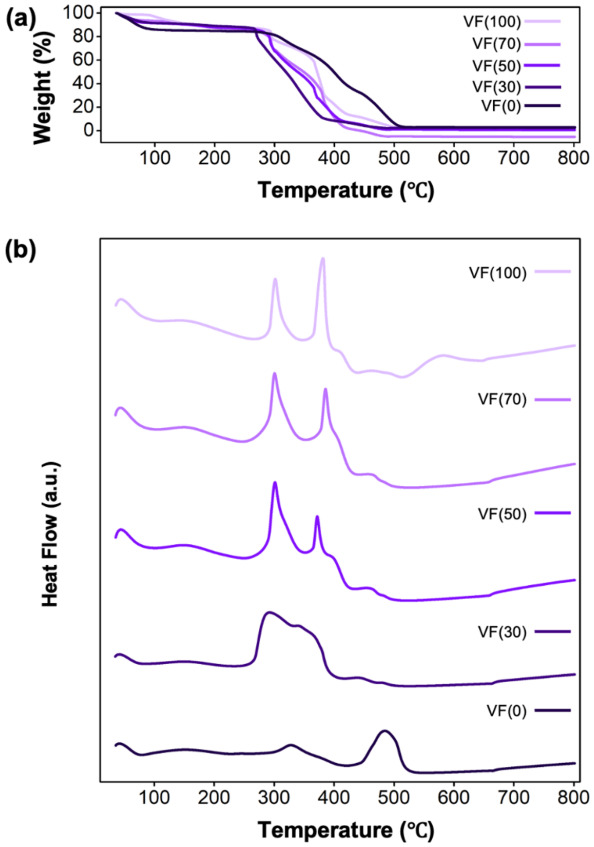


Figure 4: Thermal evolution of electrospun VF(x) nanofibers as a function of PAN content (x = 0, 30, 50, 70 and 100 wt %): (a) TGA curves and (b) DSC thermograms.

To elucidate how polymer composition modifies the surface chemistry of the V_2O_5 support, X-ray photoelectron spectroscopy (XPS) was performed on the synthesized VF(x) nanofibers (Figure 5). The V 2p spectra (Figure 5a) exhibit characteristic V^{4+} and V^{5+} components at 515.9/523.2 and 517.0/524.3 eV, respectively, in good agreement with reported values for orthorhombic V_2O_5 [29,30]. No appreciable changes in either the binding energies or relative spectral features are observed with increasing PAN content, indicating that polymer modulation does not alter the chemical state of the V_2O_5 framework, consistent with the Raman results (vide supra). In contrast, the surface carbon and nitrogen chemistries exhibit pronounced changes with polymer composition. The C 1s spectra (Figure 5b) can be deconvoluted into C–C, C–N/C–O, and C=O components centered at 284.6, 286.5, and 288.0 eV, respectively [31,32]. More importantly, the N 1s spectra (Figure 5c) show that increasing the PAN content progressively enriches the V_2O_5 surface with pyridinic nitrogen functionalities, particularly above 50 wt %. These nitrogen functionalities originate from PAN-derived oxidative stabilization during calcination, in agreement with the thermal analysis. Since pyridinic nitrogen has been reported to serve as an effective anchoring site for Ru precursor species [33], the increased abundance of pyridinic nitrogen is expected to facilitate preferential Ru nucleation during the subsequent deposition process. The evolution of the O 1s spectra (Figure 5d) further supports the polymer-induced surface reconstruction. Deconvolution of the spectra identifies lattice oxygen, oxygen-deficient species, and adsorbed oxygen at approximately 530, 531, and 533 eV, respectively [34,35]. Notably, the relative concentration of oxygen-deficient surface species increases progressively with PAN incorporation, with a pronounced increase observed above 50 wt % PAN. Consistent

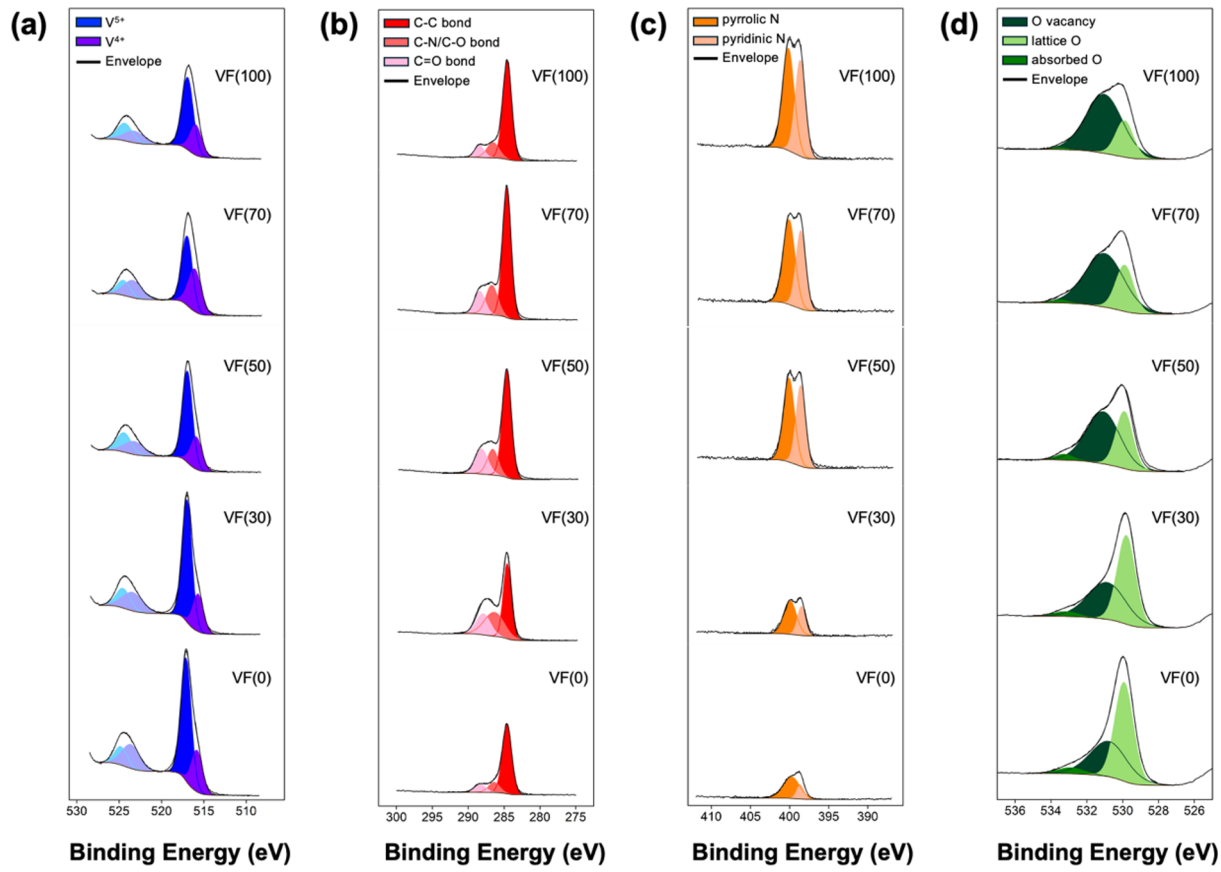


Figure 5: ARXPS spectra of VF(*x*) with increasing PAN content (*x* = 0, 30, 50, 70, and 100 wt %), showing the (a) V 2p, (b) C 1s, (c) N 1s, and (d) O 1s core-level regions.

with this trend, the oxygen-vacancy-to-lattice-oxygen ratio increases from approximately 1.2 for VF(0) and VF(30) to 1.8, 2.6, and 3.5 for VF(50), VF(70), and VF(100), respectively. The evolution of pyridinic nitrogen and oxygen-deficient surface sites closely parallels the morphological transition of RuO_2 observed by SEM and TEM, suggesting that polymer-derived surface reconstruction modifies the interfacial chemical environment governing Ru precursor adsorption and anisotropic crystal growth. Furthermore, the V^{4+} species detected by XPS may facilitate the nucleation of rutile RuO_2. Because V^{4+} can locally form rutile-type VO_2-like domains, which are isostructural with RuO_2 and have comparable lattice parameters, these domains could serve as low-mismatch templates for RuO_2 nucleation [36].

Conclusion

In this study, we developed a polymer-regulated strategy for simultaneously stabilizing electrospun V_2O_5 nanofibers and directing the anisotropic growth of RuO_2 nanorods by tuning the PVP/PAN ratio in the electrospinning precursor. By systematically tuning the PVP/PAN ratio, the thermal evolution of the precursor fibers and the resulting surface chemistry were effectively controlled while preserving the crystalline V_2O_5 framework. In particular, a PAN content of approximately 50 wt % promotes the formation of pyridinic nitrogen functionalities and oxygen-deficient surface sites, which are proposed to facilitate preferential Ru precursor nucleation and the subsequent growth of uniformly aligned RuO_2 nanorods. These findings demonstrate that polymer composition serves as an effective means of regulating interfacial chemistry during thermal processing, providing a simple and scalable strategy for controlling oxide nanostructures without relying on surfactants, templates, or complex synthetic procedures.

Supporting Information

Supporting Information File 1

Additional figures.
[https://www.beilstein-journals.org/bjnano/content/supplementary/2190-4286-17-106-S1.pdf]

Acknowledgements

D.J. gratefully acknowledge support from Department of Chemistry, College of Natural Science at Jeonbuk National University.

Funding

This work was financially supported by the National Research Foundation of Korea (NRF) funded by the Ministry of Science and ICT or by the Ministry of Education (NRF-RS-2018-NR031064, RS-2025-16063688, RS-2026-25493580, and RS-2026-25598759).

Conflict of Interest

The authors declare that they have no known competing financial interests or personal relationships that could have appeared to influence the work reported in this paper.

Author Contributions

Jiwoo Song: data curation; investigation; validation; visualization. Namhee Kim: conceptualization; formal analysis; validation; visualization. Minjae Kim: formal analysis; writing – review & editing. Myung Hwa Kim: formal analysis; funding acquisition; project administration. Dasol Jin: conceptualization; data curation; formal analysis; investigation; methodology; project administration; supervision; validation; visualization; writing – original draft; writing – review & editing.

ORCID® iDs

Namhee Kim - https://orcid.org/0009-0000-1969-4370
Myung Hwa Kim - https://orcid.org/0000-0001-7254-2886

Data Availability Statement

Data generated and analyzed during this study is available from the corresponding author upon reasonable request.

References

1. Xu, L.; Xiong, P.; Zeng, L.; Fang, Y.; Liu, R.; Liu, J.; Luo, F.; Chen, Q.; Wei, M.; Qian, Q. *Nanoscale* **2019,** *11,* 16308–16316. doi:10.1039/c9nr03574e
2. Chamakh, M.; Ayesh, A. I. *Mater. Des.* **2021,** *204,* 109678. doi:10.1016/j.matdes.2021.109678
3. Sohaimi, K.; Jaafar, J.; Rosman, N. *Malays. J. Fundam. Appl. Sci.* **2023,** *19,* 901–914.
4. Deng, R.; Wang, Z.; Tan, S.; Huang, X.; Gao, Z.; Fang, Y.; Chen, C.; Wang, R.; Xu, C.; Huang, G.; Wang, J.; Pan, F. *Chem. Eng. J.* **2024,** *489,* 151095. doi:10.1016/j.cej.2024.151095
5. Zhu, C.; Shu, J.; Wu, X.; Li, P.; Li, X. *J. Electroanal. Chem.* **2015,** *759,* 184–189. doi:10.1016/j.jelechem.2015.11.013
6. Cheah, Y. L.; Gupta, N.; Pramana, S. S.; Aravindan, V.; Wee, G.; Srinivasan, M. *J. Power Sources* **2011,** *196,* 6465–6472. doi:10.1016/j.jpowsour.2011.03.039
7. Li, S.; Qin, L.; Li, L.; Cheng, H.; Fang, G.; Zhu, Q. *Int. J. Electrochem. Sci.* **2021,** *16,* 210349. doi:10.20964/2021.03.26
8. Hou, L.; Li, Z.; Jang, H.; Wang, Y.; Cui, X.; Gu, X.; Kim, M. G.; Feng, L.; Liu, S.; Liu, X. *Adv. Energy Mater.* **2023,** *13,* 2300177. doi:10.1002/aenm.202300177
9. Liu, M.; Su, B.; Tang, Y.; Jiang, X.; Yu, A. *Adv. Energy Mater.* **2017,** *7,* 1700885. doi:10.1002/aenm.201700885
10. Chun, S. H.; Choi, H.-A.; Kang, M.; Koh, M.; Lee, N.-S.; Lee, S. C.; Lee, M.; Lee, Y.; Lee, C.; Kim, M. H. *ACS Appl. Mater. Interfaces* **2013,** *5,* 8401–8406. doi:10.1021/am4016445
11. Shahzad, U.; Saeed, M.; Marwani, H. M.; Al-Humaidi, J. Y.; Rehman, S. u.; Althomali, R. H.; Awual, M. R.; Rahman, M. M. *Crit. Rev. Anal. Chem.* **2025,** *55,* 1081–1098. doi:10.1080/10408347.2024.2337876
12. Li, T.; Yin, W.; Gao, S.; Sun, Y.; Xu, P.; Wu, S.; Kong, H.; Yang, G.; Wei, G. *Nanomaterials* **2022,** *12,* 982. doi:10.3390/nano12060982
13. Over, H. *Chem. Rev.* **2012,** *112,* 3356–3426. doi:10.1021/cr200247n
14. Hodnik, N.; Jovanovič, P.; Pavlišič, A.; Jozinović, B.; Zorko, M.; Bele, M.; Šelih, V. S.; Šala, M.; Hočevar, S.; Gaberšček, M. *J. Phys. Chem. C* **2015,** *119,* 10140–10147. doi:10.1021/acs.jpcc.5b01832
15. Wang, Y.; Cao, G. *Chem. Mater.* **2006,** *18,* 2787–2804. doi:10.1021/cm052765h
16. Inoue, Y.; Ohtsuka, S.; Torikai, T.; Watari, T.; Yada, M. *Cryst. Growth Des.* **2009,** *9,* 5092–5100. doi:10.1021/cg900261s
17. Wu, X.; Bai, W.; Yuan, L.; Li, J.; Qi, L.; Weng, X.; Gu, C.; Bi, M. *ACS Appl. Mater. Interfaces* **2025,** *17,* 19848–19855. doi:10.1021/acsami.4c10823
18. Walls, B.; Murtagh, O.; Bozhko, S. I.; Ionov, A.; Mazilkin, A. A.; Mullarkey, D.; Zhussupbekova, A.; Shulyatev, D. A.; Zhussupbekov, K.; Andreev, N.; Tabachkova, N.; Shvets, I. V. *Materials* **2022,** *15,* 7652. doi:10.3390/ma15217652
19. Park, J.; Lee, J. W.; Ye, B. U.; Chun, S. H.; Joo, S. H.; Park, H.; Lee, H.; Jeong, H. Y.; Kim, M. H.; Baik, J. M. *Sci. Rep.* **2015,** *5,* 11933. doi:10.1038/srep11933
20. Kim, S.-j.; Cho, Y. K.; Lee, C.; Kim, M. H.; Lee, Y. *Biosens. Bioelectron.* **2016,** *77,* 1144–1152. doi:10.1016/j.bios.2015.11.012
21. Kim, K.-H.; Kim, K. S.; Kim, G.-P.; Baeck, S.-H. *Curr. Appl. Phys.* **2012,** *12,* 36–39. doi:10.1016/j.cap.2011.04.029
22. Baddour-Hadjean, R.; Pereira-Ramos, J. P.; Navone, C.; Smirnov, M. *Chem. Mater.* **2008,** *20,* 1916–1923. doi:10.1021/cm702979k
23. Khodakov, A.; Olthof, B.; Bell, A. T.; Iglesia, E. *J. Catal.* **1999,** *181,* 205–216. doi:10.1006/jcat.1998.2295
24. Prasad, A.; John, M. S.; John, F. *Mater. Chem. Phys.* **2026,** *348,* 131676. doi:10.1016/j.matchemphys.2025.131676
25. Gershinsky, G.; Yoo, H. D.; Gofer, Y.; Aurbach, D. *Langmuir* **2013,** *29,* 10964–10972. doi:10.1021/la402391f
26. Elishav, O.; Beilin, V.; Rozent, O.; Shter, G. E.; Grader, G. S. *J. Polym. Sci., Part B: Polym. Phys.* **2018,** *56,* 248–254. doi:10.1002/polb.24538
27. Ucar, N.; Demirsoy, N.; Onen, A.; Karacan, I.; Kizildag, N.; Eren, O.; Faruk Vurur, O.; Sezer, E.; Ustamehmetoglu, B. *J. Mater. Sci.* **2015,** *50,* 1855–1864. doi:10.1007/s10853-014-8748-4
28. Yin, C.; Li, L.; Jia, R.; Hu, J. *Inorg. Chem.* **2024,** *63,* 20551–20561. doi:10.1021/acs.inorgchem.4c03146
29. Lin, L.; Tian, S.-L.; Fang, L.; Chang, L.-M.; Liu, W.-Q.; Wang, Q.-S. *J. Energy Storage* **2023,** *72,* 108356. doi:10.1016/j.est.2023.108356
30. Silversmit, G.; Depla, D.; Poelman, H.; Marin, G. B.; De Gryse, R. *J. Electron Spectrosc. Relat. Phenom.* **2004,** *135,* 167–175. doi:10.1016/j.elspec.2004.03.004

31. Liu, T.; Li, L.; Yao, T.; Li, Y.; Zhu, L.; Li, F.; Han, X.; Cheng, Y.; Wang, H. *Electrochim. Acta* **2021,** *369,* 137711. doi:10.1016/j.electacta.2020.137711
32. Chen, X.; Unruh, K. M.; Ni, C.; Ali, B.; Sun, Z.; Lu, Q.; Deitzel, J.; Xiao, J. Q. *J. Phys. Chem. C* **2011,** *115,* 373–378. doi:10.1021/jp1082533
33. Zhang, C.; Sha, J.; Fei, H.; Liu, M.; Yazdi, S.; Zhang, J.; Zhong, Q.; Zou, X.; Zhao, N.; Yu, H.; Jiang, Z.; Ringe, E.; Yakobson, B. I.; Dong, J.; Chen, D.; Tour, J. M. *ACS Nano* **2017,** *11,* 6930–6941. doi:10.1021/acsnano.7b02148
34. Zhao, K.; Teng, L.; Tang, Y.; Chen, X. *Ceram. Int.* **2014,** *40,* 15335–15340. doi:10.1016/j.ceramint.2014.06.079
35. Song, J.; Gu, X.; Cao, Y.; Zhang, H. *J. Mater. Chem. A* **2019,** *7,* 10543–10551. doi:10.1039/c9ta01674k
36. Kim, S.-j.; Cho, Y. K.; Seok, J.; Lee, N.-S.; Son, B.; Lee, J. W.; Baik, J. M.; Lee, C.; Lee, Y.; Kim, M. H. *ACS Appl. Mater. Interfaces* **2015,** *7,* 15321–15330. doi:10.1021/acsami.5b03178

License and Terms

This is an open access article licensed under the terms of the Beilstein-Institut Open Access License Agreement (https://www.beilstein-journals.org/bjnano/terms), which is identical to the Creative Commons Attribution 4.0 International License (https://creativecommons.org/licenses/by/4.0). The reuse of material under this license requires that the author(s), source and license are credited. Third-party material in this article could be subject to other licenses (typically indicated in the credit line), and in this case, users are required to obtain permission from the license holder to reuse the material.

The definitive version of this article is the electronic one which can be found at:
https://doi.org/10.3762/bjnano.17.106